RSC Advances

PAPER

View Article Online
View Journal | View Issue

Cite this: *RSC Adv.*, 2019, **9**, 40694

Visible-light photocatalytic capability and the mechanism investigation of a novel PANI/Sn_3O_4 p–n heterostructure†

Manfei Lv,[ab] Liuqing Yang, *[b] Xiangliang Wang,[b] Xinlei Cheng,[b] Yan Song,[b] Yinkun Yin,[b] Huimin Liu,[c] Yongjun Han,[b] Kesheng Cao,[d] Wei Ma,[b] Guang Qi[b] and Songtian Li*[ab]

Received 18th September 2019
Accepted 2nd December 2019

DOI: 10.1039/c9ra07562c

rsc.li/rsc-advances

A novel polyaniline (PANI)/Sn_3O_4 heterojunction composed of PANI nanofibers and Sn_3O_4 nanosheets was fabricated by a facile physical milling technique. Modification of Sn_3O_4 with a PANI conductive polymer contributes to facilitating interfacial charge transfer efficiency, and thus, significantly enhances the visible-light Rhodamine B (RhB) photo-degradation. Results indicate that PANI/Sn_3O_4 heterostructures with 10 wt% PANI reached the maximum degradation efficiency (around 97%) for RhB within 5 h, which is 2.27 times higher than that of Sn_3O_4 alone. This improvement is due to the p–n heterostructure formation in PANI/Sn_3O_4. Moreover, the outcome of reactive species capturing experiments demonstrated that in PANI/Sn_3O_4, holes made the largest contribution to RhB degradation under visible light illumination, while hydroxyl radicals showed less significance under the same conditions. In addition, the photocatalytic mechanism was proposed based on evidence from the reactive species test and energy band structure analysis.

1. Introduction

Rapid industrial development has generated a variety of water pollution problems that are posing serious challenges to environmental remediation. Recently, the removal of organic contaminants and decolorization of dyes in waste water have become highly significant to environmental protection,[1] as the dyes exhibit stable chemical properties, toxicity, high photostability and low biodegradability.[2] More seriously, most of these dyes will be lost during processing and discharged as waste water, which means potential harm to human beings, animals and plants. Many dyes are toxic, carcinogenic and mutagenic, such as Rhodamine B. Photocatalysis is a promising technology for water purification not only because of its low-cost, but also due to the eco-friendliness – no secondary pollution is created during the reaction process.[3] Thus, it has become a research hot spot with respect to organic contaminant degradation. Mixed-valence or non-stoichiometric tin oxide (Sn_3O_4),[4] as an n-type semiconductor, can effectively catalyze the degradation of target contaminant. Theoretical and experimental studies show that the Sn_3O_4 nanosheets have superior visible light response and photoelectric characteristics owing to the existence of oxygen vacancies.[5]

The Sn_3O_4 nanosheets' high photocatalytic activity is due to its nanocrystalline properties, mixed-valence and layered nanosheet morphology.[6] However, the visible light absorption region of pure Sn_3O_4 nanosheets is limited, and the electron–hole pairs can be inclined to quickly recombine. As such, single component Sn_3O_4 undergoes significant charge recombination at the surface throughout the majority of the photocatalyst, which hinders its stimulation of photocatalytic properties. Thus, researchers have developed and tested several methods for depressing photogenerated carrier recombination on the Sn_3O_4 surface. Previous studies have demonstrated that forming a heterojunction between Sn_3O_4 and other materials tremendously boosts photocatalytic performances. For instance, Huda *et al.* researched that Sn_3O_4/TiO_2/Ti depicted superior decomposition of acid yellow 17 under visible light irradiation;[7] while Chunmei Li *et al.* investigated the mes-Sn_3O_4/g-C_3N_4 heterostructure and determined that it dramatically enhanced TC-HCl photocatalytic degradation in water.[8]

Polyaniline (PANI), a p-type, visible-light-responsed, active semiconductor material, has attracted comprehensive attention from the research community on account of its good conductivity, non-toxicity, easy preparation, high stability, unique electrochemical property and physical behaviour.[9] In addition,

[a]*College of Chemistry, Zhengzhou University, Zhengzhou, 450001, China*
[b]*College of Chemistry and Environmental Engineering, Pingdingshan University, Pingdingshan, 467000, China*
[c]*TJU-NIMS International Collaboration Laboratory, School of Material Science and Engineering, Tianjin University, Tianjin 300072, P. R. China*
[d]*Analytical Instrumentation Center, Pingdingshan University, Pingdingshan, 467000, China*

† Electronic supplementary information (ESI) available. See DOI: 10.1039/c9ra07562c

PANI acts as a photo-sensitizer, predominantly enhancing the charge and carrier separation and migration.[10] Ma *et al.* reported that PANI/SnO_2 heterostructure with enhanced photocatalytic activity toward methyl orange.[11] Shirmardi *et al.* determined that ZnSe/PANI nanocomposite displayed photocatalytic property for the removal of methylene blue and chromate ions.[12] However, the coupling of p-type PANI with n-type Sn_3O_4 for photocatalytic application has rarely been reported until now. Given the good conductivity of PANI nanofibers, we proposed the construction of a novel PANI/Sn_3O_4 p–n heterostructure to accelerate carrier separation rate for improved photocatalytic performance. Integration of PANI and Sn_3O_4 changes the structural, optical and electronic performance of this composite material,[13] and the PANI/Sn_3O_4 obtained broader light responsive spectra and boosted the interface charge transfer effectively, which significantly enhanced the photocatalytic performance to a degree.

In this work, Sn_3O_4 nanosheets were synthesized using a general hydrothermal method, after which PANI nanofibers were prepared *via* a *in situ* polymerization process.[14] Then, using PANI nanofibers as a modified composition for Sn_3O_4 nanosheets, the p–n PANI/Sn_3O_4 heterojunction was constructed *via* a mechanical milling method. Compared to single Sn_3O_4, the PANI/Sn_3O_4 nano-heterostructure exhibited a dramatic improvement in terms of photocatalytic property and stability. It is ascribed to the mutual interaction between Sn_3O_4 and PANI in RhB degradation under visible light. Thus, this PANI/Sn_3O_4 heterostructure shows promising potential for practical application in organic pollutant degradation. This work provides a feasible and novel approach for further research on the application of polymers in the field of photocatalysis.

2. Experimental

2.1. Materials

Tin(II) dichloride dihydrate ($SnCl_2 \cdot 2H_2O$), citric acid ($C_6H_8O_7 \cdot 2H_2O$), aniline monomer ($C_6H_5NH_2$) and ammonium persulfate [$(NH_4)_2S_2O_8$] (APS) were bought from Sigma Aldrich. Hydrochloric acid (HCl), ethanol and sodium hydroxide (NaOH) were received from China National Medicines Corporation, Ltd. All the chemicals in our experiments were employed without further purification.

2.2. Synthesis

2.2.1. Synthesis of Sn_3O_4 nanosheets. Sn_3O_4 was fabricated using a hydrothermal method.[15] 20 mmol $SnCl_2 \cdot 2H_2O$ and 50 mmol $C_6H_8O_7 \cdot 2H_2O$ were together dissolved in 65 mL of DL water, then the solution was continuously stirred for 2 h. Under continuous stirring conditions, NaOH particles were added to the obtained suspension to regulate pH until neutral. Subsequently, the homogeneous solution was slowly transferred to the 100 mL Teflon-lined autoclave. Then, the autoclave was heated at 180 °C for 6 h. After hydrothermal reaction, the obtained precipitate was separated by centrifugation, and then washed several times using DL water and ethanol separately. At last, the product was dried at 35 °C for 6 h in vacuum.

2.2.2. Synthesis of PANI nanofibers. PANI nanofibers were prepared by a *in situ* chemical polymerization method.[14,16] In accordance with the standard procedure, 73 μL aniline was poured into 10 mL hydrochloric acid (1 M) and with magnetic stirring at 0–5 °C for 1 h. Then 10 mL of 1 M hydrochloric acid containing 0.18 g APS with 1 : 1 molar ratio was dripped to the above mixed solution and maintained under magnetical stirring conditions for 24 h at low temperature (0–5 °C). The product was centrifuged, washed with DL water and ethanol separately, and then dried at 40 °C for 10 h under vacuum.

2.2.3. PANI/Sn_3O_4 composite synthesis. The PANI/Sn_3O_4 composites were prepared *via* a solvent evaporation and physical milling process.[17,18] First, 10 mg PANI and 190 mg Sn_3O_4 were separately dispersed in beakers containing 30 mL DL water and sonicated for 30 minutes so as to accelerate fully dispersion. Then the suspensions containing PANI and Sn_3O_4 were mixed under stirring conditions and heated continuously in a water bath to accelerate solvent evaporation. When the solvent was completely evaporated, the composite was transferred to an oven for drying. The dried samples were ground in an agate mortar, thereby preparing the PANI/Sn_3O_4 powder with a 5% PANI mass ratio. The additional sample PANI/Sn_3O_4 hybrids with different ratios were identically prepared through varying blending ratios. The composites with different PANI weight ratios were denoted as PANI/Sn_3O_4-5%, PANI/Sn_3O_4-10%, PANI/Sn_3O_4-30% and PANI/Sn_3O_4-50%.

2.3. Characterizations

The following techniques were exploited to determine the as-prepared samples' physical and chemical properties. Fourier transform-infrared (FT-IR) spectrums were tested over the region 4000–400 cm^{-1} from a Tensor 37 with a KBr pellet. The crystal forms were measured by X-ray diffraction (XRD) named Smartlab with Cu Kα radiation (45 kV, 200 mA, $\lambda = 1.5406$ Å). Microstructures and morphologies of materials were employed by field emission scanning electron microscope (FE-SEM, Hitachi SU8010, Japan) and high resolution transmission electron microscope (HR-TEM, TecnaiG2 F20, FEI, USA) at 1 kV and 200 kV, respectively. The nitrogen adsorption–desorption isotherm was determined at 77 K (Quantachrome Instruments, Boynton Beach, FL, USA). Ultraviolet-visible diffuse reflectance spectra (UV-vis DRS) were obtained from 200–800 nm *via* a spectrometer (Shimadzu UV2600). Photoluminescence (PL) spectra were conducted on the F-7000 with 248 nm as the excitation wavelength. X-ray photoelectron spectroscopy (XPS) spectra were measured by the Thermo ESCALAB 250XI photoelectron spectroscope system using Al Kα radiation. Electron spin resonance (ESR) tests were measured using a Bruker E500 ESR spectrometer (Billerica, MA) with 5,5-dimethyl-1-pyrroline-*N*-oxide (DMPO) in methanol. Total organic carbons (TOC) were obtained on a multi N/C 2100 (Analytik Jena AG, Germany) TOC analyzer. The photocurrent response (*I*–*t*) curve was tested at 0 V, electrochemical impedance spectroscopy (EIS) was measured at open-circuit voltage with 0.01 Hz to 1000 kHz using this three-electrode cell by a Multi-Channel Autolab M204. The photocatalyst thin film on fluorine-doped tin oxide (FTO) was

usually regarded as the working electrode with irradiation area of 1 cm^2.[19] The platinum sheet and Ag/AgCl electrode were regarded as the counter electrode and reference electrode, respectively. The electrolyte was Na_2SO_4 (0.5 M) aqueous solution.

2.4. Photocatalytic Rhodamine B degradation

The samples' photocatalytic property was investigated by monitoring the Rhodamine B aqueous solution (RhB, 10 mg L^{-1}) decomposition process. Typically, 50 mg sample was poured into a 50 mL RhB solution. Then the suspension was stirred without light irradiation for 1 h to ensure the adsorption desorption-equilibrium. Subsequently, suspension was shined by a 300 W xenon lamp equipped with a 420 nm cut-off filter under continuous stirring. At pre-specified time intervals, certain aliquots were collected and then centrifuged, after that the concentration of the residual RhB aqueous solution was detected with the UV-2550 by observing the peak intensity at 554 nm. To confirm the materials' cyclic stability, after reaction the residual catalyst was collected for circular photocatalytic tests. The RhB removal efficiency was calculated as $\eta\,(\%) = (1 - C_t/C_0) \times 100$, where η (%) was the degradation efficiency, and C_0 (mg L^{-1}) and C_t (mg L^{-1}) were the initial and reaction RhB concentrations,[19] respectively.

2.5. Mechanism study

Typical active species in the degradation process, such as hydroxyl radical ($\cdot OH$), holes (h^+) and superoxide anion radicals ($\cdot O^{2-}$) could be conducted using scavengers.[20] In this test, *tert*-butyl alcohol (*t*-BuOH),[21] ethylenediaminetetraacetic acid disodium salt dihydrate (EDTA-2Na)[8] and benzoquinone (BQ)[19] were introduced into the reaction solution as $\cdot OH$, h^+ and $\cdot O^{2-}$ scavenger, respectively. The trapping experiment was similar to the process of RhB degradation, except for a certain amount of scavengers were poured into RhB aqueous solution before the addition of catalysts.

3. Results and discussion

3.1. FT-IR analysis

The FT-IR spectrum of pure PANI, Sn_3O_4 and PANI/Sn_3O_4 heterostructure are examined in Fig. 1a. PANI spectrum depicted vibration peaks at 1576, 1478, 1287, 1351, 1118 and 830 cm^{-1}.[22] The peaks at 1576 and 1478 cm^{-1} are associated with the C=C stretching vibration mode of the quinoid and benzenoid rings,[23] respectively. The peaks observed at 1287 and 1351 cm^{-1} resulted from C–N stretching, whereas the peak located at 1118 cm^{-1} corresponds to the C=N stretching of a secondary aromatic amine.[24] Finally, the peak at 830 cm^{-1} is attributed to the degree of electron delocalization and C–H out of plane vibration,[25] which corresponds to the polaron-related transition in the PANI. For the most part, these characteristic peaks correspond to PANI peak,[26] as described in literature. The characteristic Sn_3O_4 peak was observed at 486.73 cm^{-1} and represents Sn–O vibrations.[27] It was worth noting that the peak intensity of PANI/Sn_3O_4 composite was strengthened due to the introduction of PANI. The increased peak intensity might be due to the interaction between the PANI nanofibers and Sn_3O_4 nanocrystals.[28] In addition, these peaks of as-prepared samples were shifted slightly compared to their original locations in pure Sn_3O_4 samples, indicating the successful modification of mesoporous Sn_3O_4 nanosheets and PANI nanofibers.[29]

3.2. X-ray diffraction analysis

The XRD patterns of pure PANI, Sn_3O_4 and PANI/Sn_3O_4 composite are depicted in Fig. 1b. For Sn_3O_4 nanosheets, there were characteristic peaks at $2\theta = 24.10°$, 27.08°, 32.32°, 33.01°, 37.07°, 52.68°, 55.88°, 63.54°, 65.49° and 67.25° corresponding to the (101), (111), ($\bar{1}21$), (210), (130), (311), ($2\bar{4}1$), (312), ($0\bar{3}3$) and ($1\bar{3}3$) Sn_3O_4 crystal facets.[30] Thus, the peak locations are consistent with standard Sn_3O_4 (JCPDS card, no. 16-0737).[31] In addition, the average crystallite sizes were estimated from XRD peaks, and equalled 13.56 nm. The PANI nanofibers showed a peak at 15° which confirmed the polymer chain's two-dimensional arrangement.[32] And, the characteristic peak

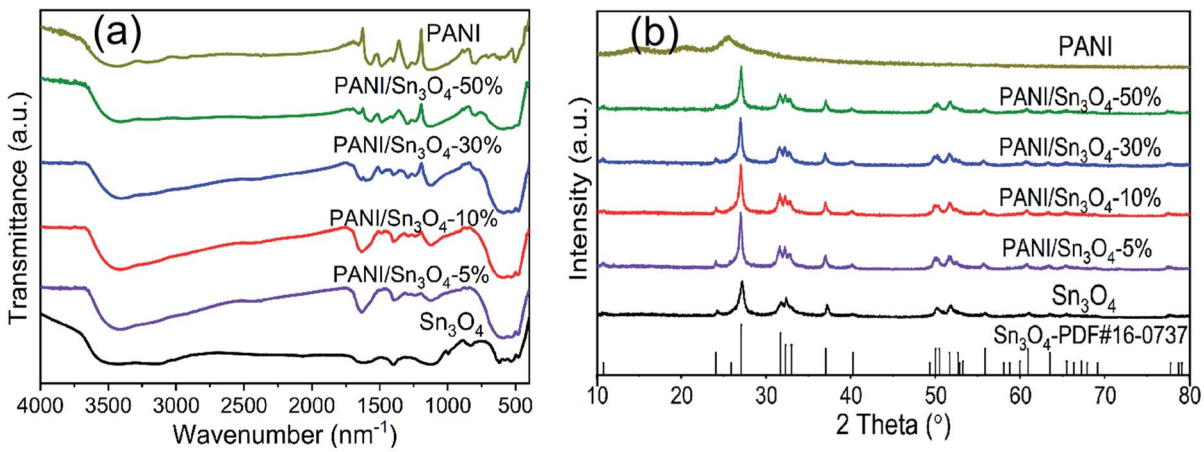

Fig. 1 (a) FT-IR spectra and (b) XRD patterns of the pure PANI, Sn_3O_4 and PANI/Sn_3O_4 composite.

detected at 25° could be due to the periodicity parallel and perpendicular to the PANI,[33,34] implying an amorphous structure of the synthesized polymer PANI.[35,36] In case of composites, no impurity peaks were detected.[29] And all the PANI/Sn_3O_4 composites had the same profile as single Sn_3O_4 owing to the fact that the crystal structure of Sn_3O_4 wasn't changed by PANI.[37]

3.3. Morphology

The prepared samples' morphology and microstructure were shown by SEM. Fig. 2a depicts a low magnification SEM image that displays distinct, hierarchical flower-like structures with a scale size of ~0.2–1.0 μm in diameter; while Fig. 2b, a high magnification image, shows Sn_3O_4 composed of numerous, thin nanoflakes with thickness ranging from 5 to 10 nm. Fig. 2c and d are FE-SEM images of PANI nanofiber with diameters ranging from 40 to 90 nm, and its lengths ranging from 0.5 to 2 μm. The PANI/Sn_3O_4-10% composites (Fig. 2e and f) exhibit PANI morphology with a short-chained fibrous structure and Sn_3O_4 nanoflakes scattered at the edge and tips of the PANI nanofibers.

The SAED pattern and high-resolution TEM of Sn_3O_4 were displayed in Fig. 3a and b. Besides, the HRTEM analysis of PANI/Sn_3O_4-10% heterostructure (Fig. 3c) was also demonstrated to know about detailed information on the morphology and structure. Presented in Fig. 3b and c, the lattice fringes with an interplanar spacing of 0.33 and 0.28 nm were attributed to the (111) and ($\bar{1}$21) crystal orientation of triclinic Sn_3O_4,[15] respectively. TEM of PANI, Sn_3O_4 and PANI/Sn_3O_4-10% hybrid were performed in Fig. 3d–g, which were consistent with SEM results. The 3D hierarchical flower-like Sn_3O_4 tended to randomly deposit on the PANI nanofibers surfaces,[38] and almost amorphous PANI nanofibers were located on the surfaces and edges of Sn_3O_4 nanosheets. Apparently, the results of HR-TEM and TEM were consistent with the XRD analysis results, which was indicative of the successful formation of PANI/Sn_3O_4 heterostructure. The EDS analysis of PANI/Sn_3O_4-10% composite was performed in Fig. 3h–k, which symbolized the existence of C, N, O and Sn elements in heterojunction, and Sn_3O_4 nanosheets were adhered well on the surface of PANI nanofibers.[39] With the aggregation of Sn_3O_4 nanosheets self-assembled, the amount of reflected light within the interconnected nanoflakes multiplies, which improves the hierarchical structure's light absorption capacity.[40] Significantly, PANI nanofibers as light-harvesting materials, it could drastically

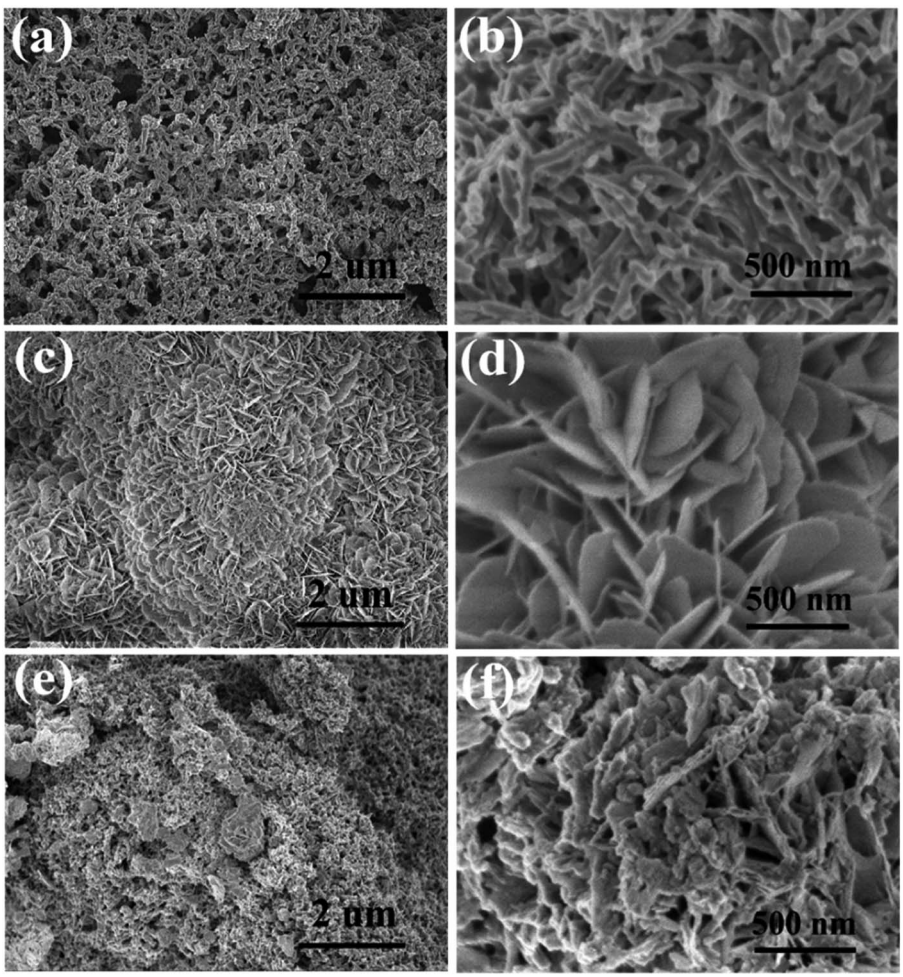

Fig. 2 SEM images of the PANI (a and b), Sn_3O_4 (c and d) and PANI/Sn_3O_4-10% heterostructures (e and f).

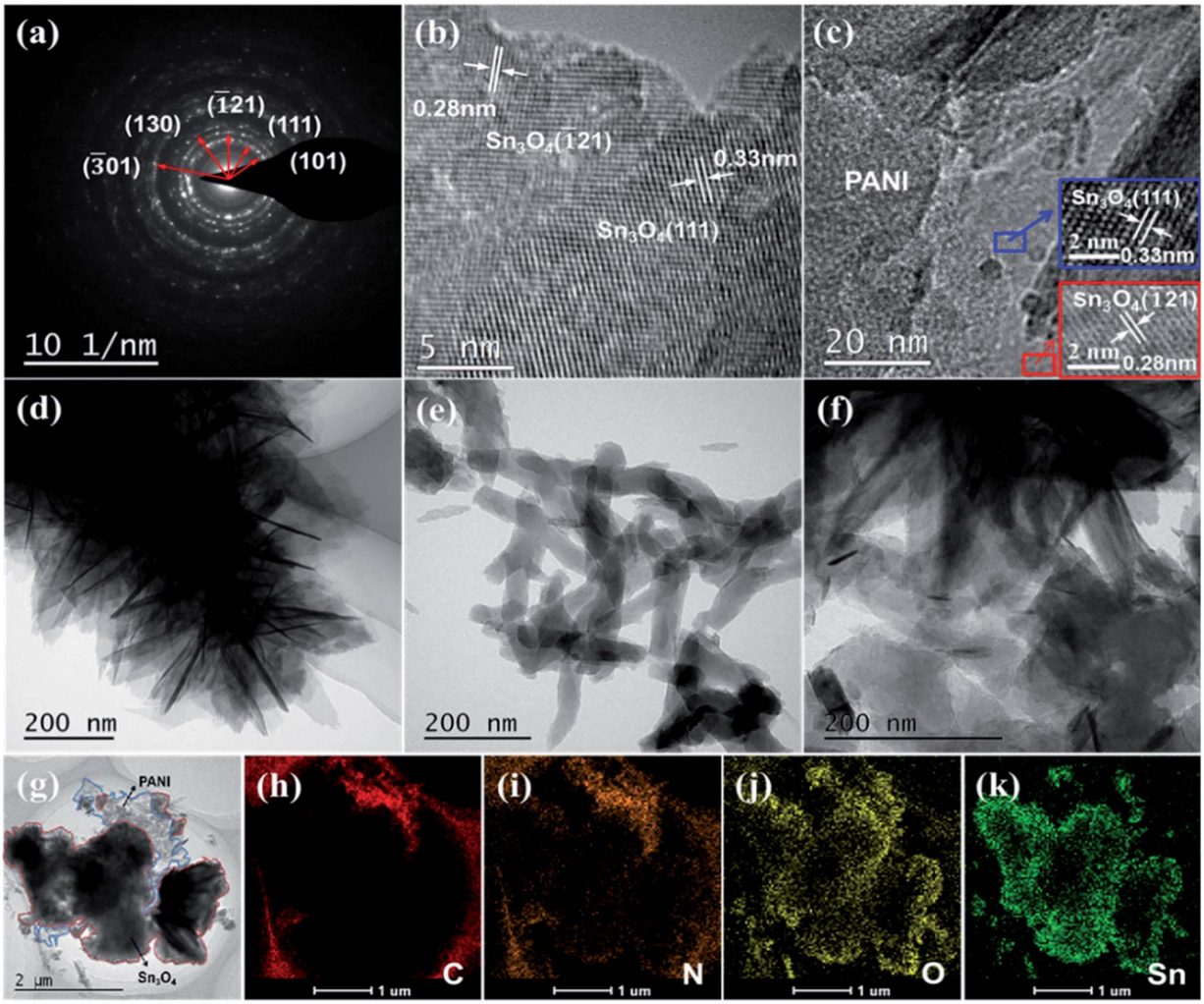

Fig. 3 SAED pattern and HRTEM image of Sn_3O_4 (a and b), HRTEM image of PANI/Sn_3O_4-10% (c); TEM images of pristine Sn_3O_4 (d), PANI nanofibers (e), PANI/Sn_3O_4-10% hybrid (f and g); EDS mapping of PANI/Sn_3O_4-10% heterostructure (h–k).

strengthen the light absorption for PANI/Sn_3O_4 heterostructure, which could dramatically facilitate the separation and transmission of photoinduced carriers,[19] further increasing the photocatalytic performances.

3.4. XPS analysis

XPS spectra is used to analyze the valence states and superficial chemical ingredient of PANI/Sn_3O_4-10% heterostructure.[41] Fig. 4a showed that the Sn 3d in PANI/Sn_3O_4 composite were decomposed into two bimodal peaks, respectively. And the peaks displayed at 495.02 and 486.56 eV were assigned to Sn(II), while the peaks of 487.03 and 495.51 eV were ascribed to Sn(IV).[42] The O 1s spectra of PANI/Sn_3O_4-10% exhibited in Fig. 4b were fitted into two peaks at 530.57 and 531.67 eV, which could be assigned to the lattice oxygen bounded to tin atoms (Sn–O) and induced by the oxygen vacancies[43] within the composites, respectively. As for the N 1s spectrum (Fig. 4c), the main peak line could be dissolved into four peak line. The peaks corresponding to quinoid di-imine nitrogen and benzenoid diamine nitrogen[44] were located at 398.54 and 399.52 eV, respectively. The peaks displayed at 401.19 and 402.69 eV could be attributed to oxidized amine and protonated imine,[45] respectively. In Fig. 4d, the C 1s spectra of PANI/Sn_3O_4-10% composite was deconvoluted into five peaks located at 284.57, 285.15, 285.78, 286.67 and 288.95 eV. The first four peaks were associated with the C–C/C–H, C–N/C=N, C–N^+/C=N^+/C–Cl and C=O/C–O,[45] respectively. In addition, the peak at 288.95 eV could be due to the oxygen-containing functional groups.[46,47] This might be owing to the formation of new chemical bonds in PANI/Sn_3O_4-10% heterostructure, *i.e.*, the PANI nanofibers were chemical bounded on the surface of Sn_3O_4 nanoflakes by C–O–Sn bonds in PANI/Sn_3O_4-10% p–n hybrids.[15] Fig. 4e showed the survey spectra of PANI/Sn_3O_4-10% hybrid using bare PANI and Sn_3O_4 as comparisons. As we can see, the peaks of C 1s and N 1s were observed for PANI, while Sn_3O_4 revealed many peaks attributed to tin, oxygen and adventitious carbon from test.[15] In the survey spectrum of PANI/Sn_3O_4-10%, it was similar to that of bare Sn_3O_4 except that the peak of N 1s and C 1s for PANI/Sn_3O_4-10%

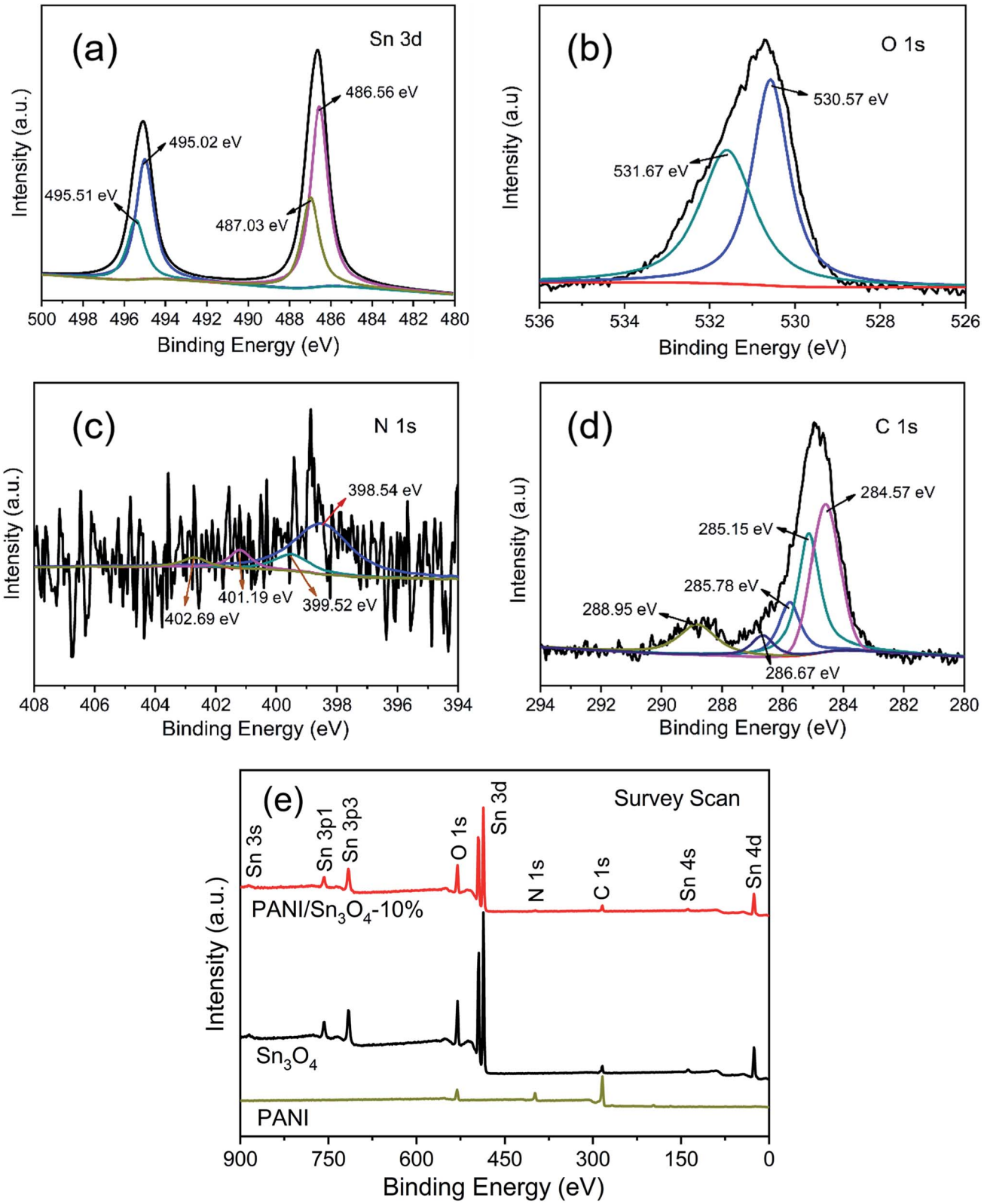

Fig. 4 The high-resolution XPS spectra of (a) Sn 3d, (b) O 1s, (c) N 1s, (d) C 1s of PANI/Sn_3O_4-10% composite and (e) survey XPS spectra of pristine PANI, Sn_3O_4 and PANI/Sn_3O_4-10% hybrid.

composite originates from the introduction of PANI nanofibers. The survey spectrum indicated that PANI/Sn_3O_4-10% hybrid was consist of Sn, O, C and N elements, confirming the successful fabrication of PANI/Sn_3O_4 p–n heterostructure. These results are well in agreement with the HR-TEM and EDS mapping analysis.[48]

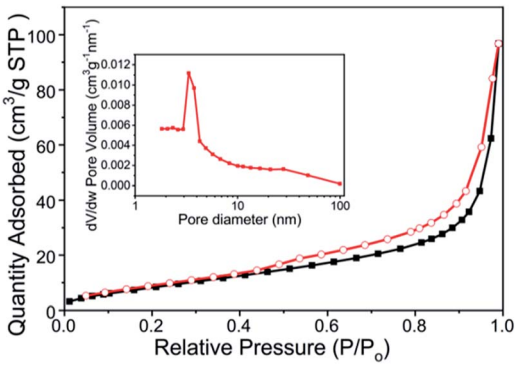

Fig. 5 N_2 adsorption–desorption isotherms of PANI/Sn_3O_4-10% nanocomposites. Inset is the hierarchical PANI/Sn_3O_4-10% pore-size distribution.

3.5. Burnauer–Emmett–Teller (BET) analysis

It has been well established that photocatalytic property is dependent on the BET surface area and porosity of nanoscale materials. The BET surface area, pore volume and average pore size of all materials are displayed in ESI Table S1.† PANI showed a stronger adsorption ability, which was in good agreement with the larger specific surface area (Fig. S1(a), ESI†). Moreover, the PANI's better adsorption capability might be related to the adsorption of imines in its molecular chain, which effectively improved the adsorption and degradation of organic contaminant for PANI/Sn_3O_4 composite. Fig. 5 showed that the PANI/Sn_3O_4-10% composite's N_2 adsorption/desorption behaviour parallels that of a typical IV isotherm, and depicted type H_3 shaped hysteresis loops.[8] And the pore size distribution and N_2 adsorption–desorption curves with different weight ratio of PANI in composite materials were provided (Fig. S1(c–f), ESI†). The enlarged BET surface area and pore volume of the PANI/Sn_3O_4 composites, relative to bare Sn_3O_4, can exhibit better adsorption ability, leading to that heterostructure may supply more surface reaction sites.[49] For highly mesoporous materials, a hysteresis loop was observed owing to capillary condensation.[50] Such a self-organized mesoporous structure could be important in photocatalysis, as it provides efficient transmission path for reactant and product molecules.[51] The mesoporous structures of PANI/Sn_3O_4 composite promote absorption of additional dye molecules, which is favourable to the dye degradation process. Therefore, compared to Sn_3O_4 nanosheets, the PANI/Sn_3O_4 composite is expected to exhibit predominant photocatalytic performance.

3.6. UV-vis analysis

The PANI, Sn_3O_4 nanosheets and the PANI/Sn_3O_4 heterostructure' light absorption properties are shown in Fig. 6a. The Sn_3O_4 sample showed photoabsorption capability from UV to visible region, with a light absorption edge of ~506 nm. With the mass ratio increase of polyaniline in composites, the peak shifts toward the higher wavelength which means that the optical absorption range of PANI/Sn_3O_4 composites also increase gradually, *i.e.*, the composite's light absorption ability has been strengthened than that of pure Sn_3O_4 in visible region. Moreover, the PANI/Sn_3O_4 heterostructure absorbed more visible light, probably owing to the light absorption of PANI in composite that could be assigned to the polaron transition,[52] which was a typical characterization of conductive polymer PANI. The Tauc equation was employed (eqn (1)) to quantitatively estimate the optical band gap.

$$\alpha h\nu = A(h\nu - E_g)^2 \quad (1)$$

where α is the absorption coefficient, E_g is the optical band gap, $h\nu$ is the photon energy, and A is a constant that does not depend on the photon energy.[8] Until now, the Sn_3O_4 band gap was reported as ~2.61 eV,[53] 2.75 eV,[54] 2.85 eV [55] and 2.56 eV.[56] The PANI nanofibers' band gap has been reported as ~2.80 eV[57] by many researchers. The Tauc plots in Fig. 6b indicated that the optical band gap value of Sn_3O_4 and PANI/Sn_3O_4-10% samples were 2.56 eV and 2.06 eV, respectively. Therefore, the composite was effectively doped with PANI performing the role of the photosensitizer. Such results indicate that the heterojunction better utilizes visible energy, and subsequently increased the photocatalytic efficiency.

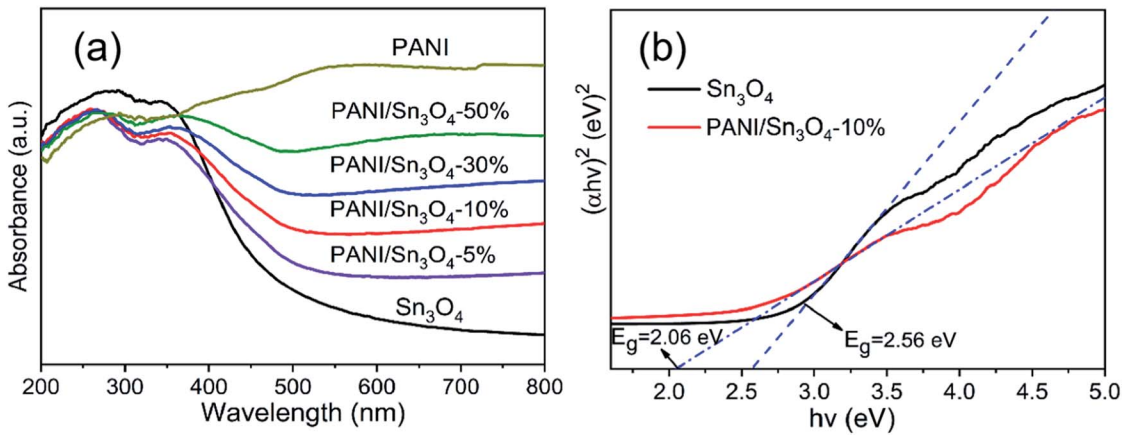

Fig. 6 (a) UV-vis DRS of PANI, Sn_3O_4 and PANI/Sn_3O_4 heterostructures and (b) Tauc plots of Sn_3O_4 and PANI/Sn_3O_4-10% heterostructure.

3.7. Photocatalytic activity of hybrid PANI/Sn_3O_4 composite

The photocatalytic property of materials was assessed by decomposing RhB dye under visible light illumination. In Fig. 7a, the residual concentration of RhB solution decreased with the time of visible light illumination increased. When the weight ratio of PANI in PANI/Sn_3O_4 was <10%, photocatalytic activity in the PANI/Sn_3O_4 increased with the continuously increasing PANI weight ratio; but the degradation rate decreased when the weight ratio of PANI in PANI/Sn_3O_4 was >10%. The results showed that the loading amount of PANI relative to Sn_3O_4 had a significant impact on the photocatalytic performance.[58] In Fig. 7b, the PANI/Sn_3O_4-10% composite exhibited the best photocatalytic activity when the PANI mass ratio reached 10%. Using this composite, 96.84% of the RhB was degraded in 5 h, which is faster than the pure Sn_3O_4 (42.71%). In general, the improved photocatalytic performance of polymer-inorganic composite could mainly be caused from the synergistic effect of PANI and Sn_3O_4. According to literature research, the performance comparison of relevant catalyst for organic dyes degradation as presented in ESI Table S2.† Results showed that the PANI/Sn_3O_4 were still competitive among the listed photocatalysts for organic dyes degradation to some extent. Simultaneously, our research group will continue to study and enhance the photocatalytic property. The UV-visible absorption spectrum of PANI/Sn_3O_4-10% showing RhB dye photocatalytic degradation was shown in Fig. 7c. The RhB dye's absorption peak intensity decreased and blue shift indicated that the chromophore group in RhB molecule structure was destroyed by PANI/Sn_3O_4-10% composite during the reaction.[59] As the decolorization doesn't signify that the dyes have been completely oxidized into harmless final products.[60] Therefore, the total organic carbon (TOC) analysis was performed on dispersions at initial and final visible-light irradiation time points. The TOC concentration decreased from 8.42 mg L^{-1} to 2.24 mg L^{-1} after the photodegradation process over PANI/Sn_3O_4-10% for 5 h, *i.e.*, TOC removal achieved 73.40%, indicating that RhB degradation was accompanied by partial mineralization.[61] It is noteworthy that mechanical blends dramatically improved the photocatalytic activity to some extent, which could be related to the photoelectron energy in terms of dye degradation and the adsorption behaviour on the conducting polymer's surface.[62] The conducting polymer PANI has shown a strong photoresponse in visible region, which has the high capacity photogenerated holes. Importantly, PANI nanofibers act as a limited delayed-action part in the PANI/Sn_3O_4 composite by offering a transition platform for photoelectrons. Thus, it has been demonstrated that conductive polymer PANI nanofibers perform an essential role in enhancing photocatalytic property, as PANI decreases recombination of photoinduced carriers and boosts effectively charge transfer in PANI/Sn_3O_4 composite.

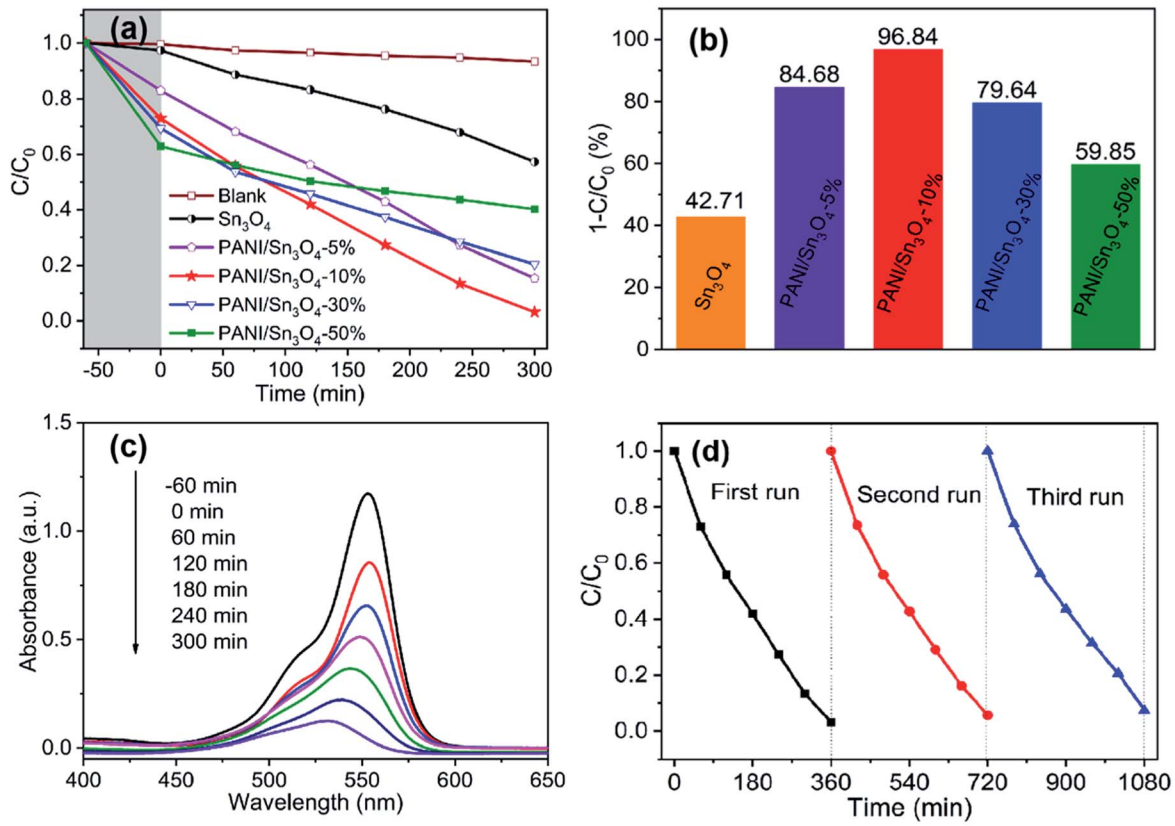

Fig. 7 (a) Photocatalytic RhB degradation curves of synthesized samples under visible light irradiation; (b) photocatalytic performance of PANI/Sn_3O_4 composite with different PANI mass ratios on RhB dye degradation; (c) temporal evolution of the RhB absorption spectra; (d) cycling runs for RhB photo-degradation of PANI/Sn_3O_4-10% under visible light irradiation.

3.8. Photocatalytic stability

RhB degradation recycling experiment was conducted on PANI/Sn_3O_4-10% to evaluate the reuse efficiency under visible light irradiation after its initial use. Fig. 7d showed that the photocatalytic performance of PANI/Sn_3O_4-10% did not significantly decrease after three runs. In fact, the degradation rate of RhB could decrease to 92.44% from maximum 96.84%. This decline might be owing to the loss of weight in washing catalyst process. The results showed PANI/Sn_3O_4-10% exhibited relatively stable photocatalytic activity during RhB photodegradation.

3.9. Charge transport and separation

The separation efficiency of photoexcited carriers acts as a decisive part in photocatalytic process. To testify the photocatalytic mechanism rationality, transient photocurrent, EIS and photoluminescence were all employed,[63] respectively. The transient photocurrent responses of Sn_3O_4 and PANI/Sn_3O_4-10% were depicted in Fig. 8a. When illuminated by visible light, the photo-current density over PANI/Sn_3O_4-10% composite was increased significantly,[64] but then dropped rapidly when turned off the light. The enhanced photocurrent of PANI/Sn_3O_4 hybrid may due to the improved transition of photoinduced carriers *via* the conductive polymer PANI. EIS study is a powerful path to study the carriers transfer and separation efficiency.[65] And it was also investigated to detect conductivity of the Sn_3O_4 and PANI/Sn_3O_4-10%. As we know, the semi-arc shape reflects the speed of electron transmission.[66] In Fig. 8b, Nyquist arc radii of PANI/Sn_3O_4-10% composite was smaller than that of bare Sn_3O_4, and it signified that PANI/Sn_3O_4-10% heterostructure could receive less resistance for transport of interfacial electrons and holes compared with pure Sn_3O_4.[67] In short, the promoted photocatalytic property is chiefly owing to the excellent interfacial charge separation.[68]

Generally speaking, the photoluminescence spectra can intuitively provide information on the separation and recombination of photoexcited carriers. In Fig. 9a, the PANI/Sn_3O_4-10% heterostructure shows a low fluorescence intensity relative to Sn_3O_4. Thus, the photocatalytic performance of PANI/Sn_3O_4-10% is evidently improved with modification by the conductive polymer PANI, which restrains the recombination and boosts the separation efficiency of photo-excited carriers to some extent.

3.9.1. Photodegradation mechanism. In photocatalytic process, $\cdot O^{2-}$, $\cdot OH$ and h^+ are usually served as active species that eventually oxidize contaminants.[69] Thus, in order to verify and analyze the radical intermediate products during this photocatalytic reaction, ESR tests were performed. In Fig. 10a and b, no characteristic signals were detected in darkness, signifying radicals were generated in photocatalytic process.[39] The characteristic peak signals of $DMPO^-\cdot OH$ and $DMPO^-\cdot O^{2-}$ appeared when the PANI/Sn_3O_4-10% composites were exposed to visible illumination.[70] What's more, the characteristic signals' intensity gradually increased with illumination time. Thus, the existence of hydroxyl and superoxide radicals in the reaction system was confirmed. In this work, trapping experiments investigated active species generation, as well as their impact on the degradation course.[19,71] Fig. 9b showed that the RhB degradation ratio decreased when BQ, *t*-BuOH and EDTA-2Na, respectively, were added to the PANI/Sn_3O_4-10% photocatalyst reaction system. More importantly, the RhB photocatalytic degradation efficiency dropped significantly when EDTA-2Na was added, which strongly indicated that h^+ was primary reactive species in the degradation process. Similarly, RhB degradation decreased sharply after the addition of the scavenger BQ. By contrast, when *t*-BuOH was poured into the reaction system, the photodegradation process decelerated slowly, indicating that $\cdot OH$ had less influence on the system. Consequently, h^+ and $\cdot O^{2-}$ have a strong oxidation ability, which induces the photocatalytic degradation of organic contaminant.

Based on the experimental conclusion of photocatalytic degradation, photoelectrochemical test and photogenerated carrier trapping, the mechanism of RhB photo-degradation was proposed. We suggest that the promotion of photocatalytic performance is mainly due to PANI and Sn_3O_4 mixing, which improves the charge separation efficiency. In the PANI/Sn_3O_4 hybrid systems, PANI nanofibers serve as a dispersing template,

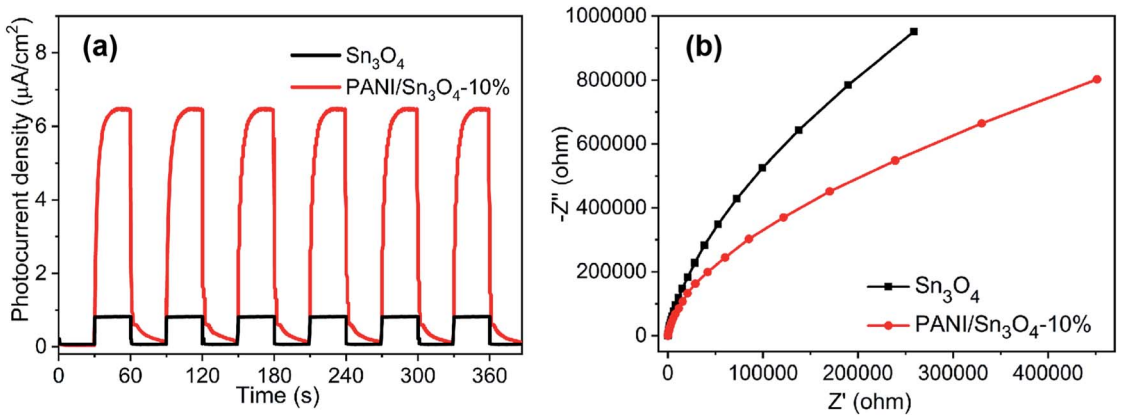

Fig. 8 (a) Instant photo-current density of the synthetic samples under visible light illumination; (b) EIS spectra of Sn_3O_4 and PANI/Sn_3O_4-10% measured at open-circuit voltage.

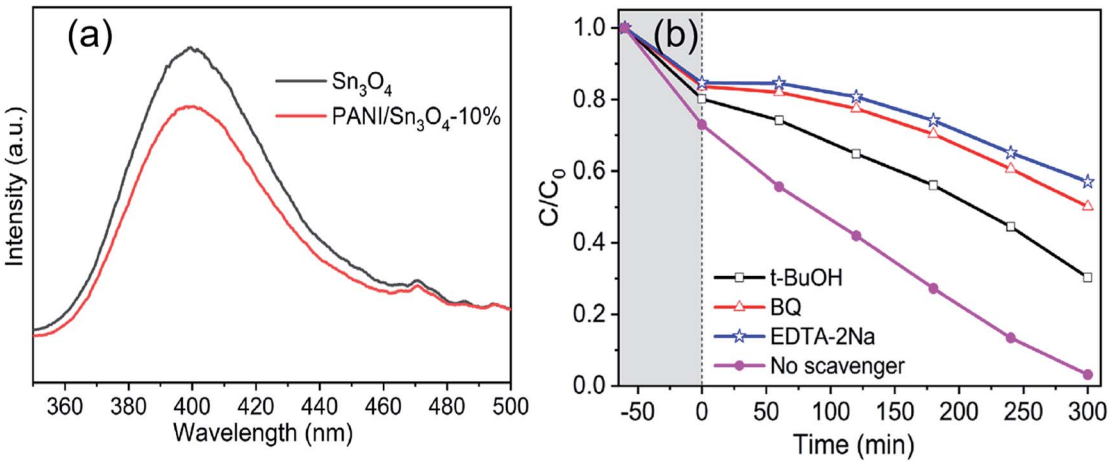

Fig. 9 (a) PL emission spectra of Sn_3O_4 and PANI/Sn_3O_4-10% composite; (b) photocatalytic performance of PANI/Sn_3O_4-10% to RhB solutions with the addition of different radical trapping agents under visible irradiation.

hole acceptors and transfer channels; and the PANI/Sn_3O_4 heterojunction synergetic effect depresses recombination of the photo-induced charge carriers.[72] The electronic and energy band structure of materials play a crucial part in properties.[73] Fig. 11 shows the carriers separation mechanism and photocatalytic reaction on the PANI/Sn_3O_4 composite. Previous literature have reported the PANI optical band gap value to be 2.70 eV;[74] while according to the experimental results, Sn_3O_4 band gap was 2.56 eV.[56] The literature reports that PANI's lowest unoccupied molecular orbital level (LUMO) (−1.90 eV) is lower than the Sn_3O_4 conduction position (−1.11 eV);[30,57] whereas Sn_3O_4 valence position (+1.46 eV) is higher than that of PANI (+0.8 eV).[30,75] Thus, the PANI's LUMO level is more negative than the Sn_3O_4 nanosheet conduction band position, and Sn_3O_4 can be used as a photoelectron sink in hybrid composite.[21] The Sn_3O_4 valence band is more positive than PANI's highest occupied molecular orbital, so PANI can be used as the acceptor of photogenerated holes for composite to some extent. When light falls on the surface of a composite catalyst, the conductive polymer PANI generates a π–π* transition,[11] delivering the excited electrons to Sn_3O_4 nanosheets' CB, after which the electrons are transferred to the photocatalysts' surface to react with oxygen. Moreover, the PANI is also a better material for hole migration.[76] The photogenerated holes in the Sn_3O_4 VB transfer to PANI's HOMO orbital,[72] then emigrate to the surface of photocatalysts.[21] In this way, the photogenerated carriers could be efficiently separated, indicating the benefit of applying the coupled system.[28] RhB is excited to RhB* under visible light illumination,[41] followed by photoinduced electron transfer from RhB* to CB of Sn_3O_4,[28] which is scavenged by dissolved O_2 to form superoxide radical anion owing to the fact that the CB position of both Sn_3O_4 and PANI located above the reduction potential of $O_2/\cdot O^{2-}$.[77] The hydroxyl radicals are produced owing to the reaction of holes with H_2O.[28] The reaction yields ·OH and $\cdot O^{2-}$ that are able to oxidize the adsorbed contaminant and form colorless small degraded products.[78] The introduce of PANI nanofibers not only improved light absorption range of PANI/Sn_3O_4 heterostructure, but also initiated the synergistic effect between Sn_3O_4 and PANI. Importantly, this might be due to the p–n junction formation at the Sn_3O_4 and

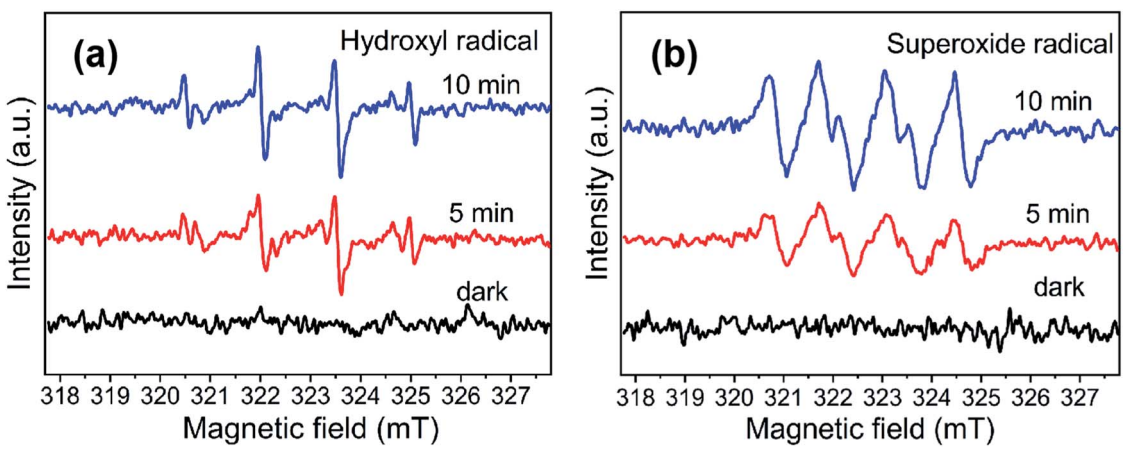

Fig. 10 ESR signals of (a) $DMPO^-\cdot OH$ and (b) $DMPO^-\cdot O^{2-}$.

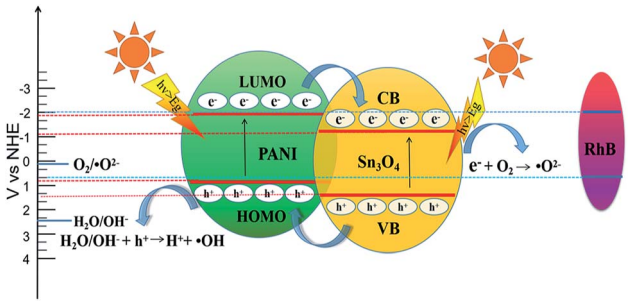

Fig. 11 Schematic representation of the photocatalytic mechanism.

PANI interface, which facilitates the transfer of photogenerated carriers. The photogenerated electron–hole pairs were effectively inhibited, which improved the photocatalytic performance.

4. Conclusions

In summary, a novel PANI/Sn_3O_4 catalyst, that effectively improves photocatalytic activity, was successfully synthesized using mechanical blends. Compared with pure Sn_3O_4, the PANI nanofibers introduced in PANI/Sn_3O_4 heterostructure reduced the agglomeration of Sn_3O_4 nanosheets.[79] Furthermore, the PANI acted as an integral part in facilitating the charge separation efficiency and photocatalytic activities of PANI/Sn_3O_4 composite due to the PANI nanofibers' high conductivity. It has been demonstrated that PANI nanofibers ensured sufficient light absorption, dye molecular adsorption and electron transfer, also provided good conductive channels to enhance photosensitive reactions in PANI/Sn_3O_4 composite. The p–n heterostructure electrical field built at the PANI/Sn_3O_4 interface and the interface housing photoinduced carriers at the energy band level between that of PANI and Sn_3O_4 have accelerated the separation of photoinduced hole–electron pairs and effectively improved photocatalytic activity. Thus, this PANI/Sn_3O_4 p–n heterojunction could be applied as an efficient photocatalyst for organic pollutants decomposition under visible light. This concept shows good application prospects in environmental purification and has the potential to be implemented on an industrial level in the future.

Conflicts of interest

There are no conflicts to declare.

Acknowledgements

Financial support from National Natural Science Foundation of China (No. 21902081), Science and Technology Key Project of Henan Province (No. 192102210031, No. 172102210429), Doctoral Scientific Research start-up Foundation of Pingdingshan University (No. PXY-BSQD-2018026) and National Scientific Research Project Cultivating Foundation of Pingdingshan University (No. PXY-PYJJ-2019004) are gratefully acknowledged.

References

1 M. Mitra, S. T. Ahamed, A. Ghosh, A. Mondal, K. Kargupta, S. Ganguly and D. Banerjee, Polyaniline/Reduced Graphene Oxide Composite-Enhanced Visible-Light-Driven Photocatalytic Activity for the Degradation of Organic Dyes, *ACS Omega*, 2019, **4**, 1623–1635.

2 S. Kalikeri, N. Kamath, D. J. Gadgil and V. S. Kodialbail, Visible light-induced photocatalytic degradation of reactive Blue-19 over highly efficient polyaniline-TiO_2 nanocomposite: a comparative study with solar and UV photocatalysis, *Environ. Sci. Pollut. Res.*, 2018, **25**, 3731–3744.

3 X. Ji, C. Bai, Q. Zhao and A. Wang, Facile synthesis of porous SnO_2 quasi-nanospheres for photocatalytic degradation of Rhodamine B, *Mater. Lett.*, 2017, **189**, 58–61.

4 W. Xia, H. Qian, X. Zeng, J. Dong, J. Wang and Q. Xu, Visible-light self-powered photodetector and recoverable photocatalyst fabricated from vertically aligned Sn_3O_4 nanoflakes on carbon paper, *J. Phys. Chem. C*, 2017, **121**, 19036–19043.

5 W. Xia, H. Qian, X. Zeng, J. Sun, P. Wang, M. Luo and J. Dong, TiO_2@Sn_3O_4 nanorods vertically aligned on carbon fiber papers for enhanced photoelectrochemical performance, *RSC Adv.*, 2019, **9**, 23334–23342.

6 S. Balgude, Y. Sethi, B. Kale, D. Amalnerkar and P. Adhyapak, Sn_3O_4 microballs as highly efficient photocatalyst for hydrogen generation and degradation of phenol under solar light irradiation, *Mater. Chem. Phys.*, 2019, **221**, 493–500.

7 A. Huda, P. Suman, L. Torquato, B. F. Silva, C. Handoko, F. Gulo, M. Zanoni and M. Orlandi, Visible light-driven photoelectrocatalytic degradation of acid yellow 17 using Sn_3O_4 flower-like thin films supported on Ti substrate (Sn_3O_4/TiO_2/Ti), *J. Photochem. Photobiol., A*, 2019, **376**, 196–205.

8 C. Li, S. Yu, H. Dong, C. Liu, H. Wu, H. Che and G. Chen, Z-scheme mesoporous photocatalyst constructed by modification of Sn_3O_4 nanoclusters on g-C_3N_4 nanosheets with improved photocatalytic performance and mechanism insight, *Appl. Catal., B*, 2018, **238**, 284–293.

9 F. Akti, Photocatalytic degradation of remazol yellow using polyaniline–doped tin oxide hybrid photocatalysts with diatomite support, *Appl. Surf. Sci.*, 2018, **455**, 931–939.

10 Y. Lin, S. Wu, C. Yang, M. Chen and X. Li, Preparation of size-controlled silver phosphate catalysts and their enhanced photocatalysis performance *via* synergetic effect with MWCNTs and PANI, *Appl. Catal., B*, 2019, **245**, 71–86.

11 H. Ma, C. Li, J. Yin, X. Pu, D. Zhang, C. Su, X. Wang and X. Shao, Polyoxometalate enhances the photocatalytic performance of polyaniline/SnO_2 composites, *Mater. Lett.*, 2016, **168**, 103–106.

12 A. Shirmardi, M. A. M. Teridi, H. R. Azimi, J. B. Wan, F. Jamali-Sheini and R. Yousefi, Enhanced photocatalytic performance of ZnSe/PANI nanocomposites for degradation of organic and inorganic pollutants, *Appl. Surf. Sci.*, 2018, **462**, 730–738.

13 J. Li, T. Peng, Y. Zhang, C. Zhou and A. Zhu, Polyaniline modified SnO_2 nanoparticles for efficient photocatalytic reduction of aqueous Cr(VI) under visible light, *Sep. Purif. Technol.*, 2018, **201**, 120–129.

14 J. Huang and R. B. Kaner, Nanofiber formation in the chemical polymerization of aniline: a mechanistic study, *Angew. Chem., Int. Ed.*, 2004, **43**, 5817–5821.

15 M. Sun, T. Yan, W. Tingting, Y. He, Y. Shao, D. Wei and D. Bin, Self-assembled hierarchical Sn_3O_4-multi-wall carbon nanotubes: facile fabrication, promoted charge separation, and enhanced photocatalytic performances, *Mater. Res. Bull.*, 2018, **103**, 104–113.

16 G. Ćirić-Marjanović, Recent advances in polyaniline research: polymerization mechanisms, structural aspects, properties and applications, *Synth. Met.*, 2013, **177**, 1–47.

17 C. Murugan, E. Subramanian and D. P. Padiyan, p–n heterojunction formation in polyaniline–SnO_2 organic–inorganic hybrid composite materials leading to enhancement in sensor functionality toward benzene and toluene vapors at room temperature, *Synth. Met.*, 2014, **192**, 106–112.

18 F. Chen, W. An, Y. Li, Y. Liang and W. Cui, Fabricating 3D porous PANI/TiO_2–graphene hydrogel for the enhanced UV-light photocatalytic degradation of BPA, *Appl. Surf. Sci.*, 2018, **427**, 123–132.

19 C. Chang, H. Yang, W. Mu, Y. Cai, L. Wang, L. Yang and H. Qin, In situ fabrication of bismuth oxyiodide ($Bi_7O_9I_3$/Bi_5O_7I) n–n heterojunction for enhanced degradation of triclosan (TCS) under simulated solar light irradiation, *Appl. Catal., B*, 2019, **254**, 647–658.

20 X. Li, J. Xiong, J. Huang, Z. Feng and J. Luo, Novel g-C_3N_4/h′$ZnTiO_3$-a′TiO_2 direct Z-scheme heterojunction with significantly enhanced visible-light photocatalytic activity, *J. Alloys Compd.*, 2019, **774**, 768–778.

21 H. Zhang, R. Zong, J. Zhao and Y. Zhu, Dramatic visible photocatalytic degradation performances due to synergetic effect of TiO_2 with PANI, *Environ. Sci. Technol.*, 2008, **42**, 3803–3807.

22 S. Rajaboopathi and S. Thambidurai, Heterostructure of CdO-ZnO nanoparticles intercalated on PANI matrix for better thermal and electrochemical performance, *Mater. Sci. Semicond. Process.*, 2017, **59**, 56–67.

23 H. Ma, Y. Luo, S. Yang, X. Li, F. Cao and J. Gong, Synthesis of aligned polyaniline belts by interfacial control approach, *J. Phys. Chem. C*, 2011, **115**, 12048–12053.

24 X. Jing, Y. Wang, D. Wu and J. Qiang, Sonochemical synthesis of polyaniline nanofibers, *Ultrason. Sonochem.*, 2007, **14**, 75–80.

25 S. Xing, C. Zhao, S. Jing and Z. Wang, Morphology and conductivity of polyaniline nanofibers prepared by seeding polymerization, *Polymer*, 2006, **47**, 2305–2313.

26 X. Chen, H. Li, H. Wu, Y. Wu, Y. Shang, J. Pan and X. Xiong, Fabrication of TiO_2@PANI nanobelts with the enhanced absorption and photocatalytic performance under visible light, *Mater. Lett.*, 2016, **172**, 52–55.

27 R. Pandimurugan and S. Thambidurai, Synthesis of seaweed-ZnO-PANI hybrid composite for adsorption of methylene blue dye, *J. Environ. Chem. Eng.*, 2016, **4**, 1332–1347.

28 M. J. Chatterjee, S. T. Ahamed, M. Mitra, C. Kulsi, A. Mondal and D. Banerjee, Visible-light influenced photocatalytic activity of polyaniline-bismuth selenide composites for the degradation of methyl orange, rhodamine B and malachite green dyes, *Appl. Surf. Sci.*, 2019, **470**, 472–483.

29 Q. Wang, Q. Zong, C. Zhang, H. Yang and Q. Zhang, Network structure of SnO_2 hollow sphere/PANI nanocomposites for electrochemical performance, *Dalton Trans.*, 2018, **47**, 2368–2375.

30 Y. He, D. Li, J. Chen, Y. Shao, J. Xian, X. Zheng and P. Wang, Sn_3O_4: a novel heterovalent-tin photocatalyst with hierarchical 3D nanostructures under visible light, *RSC Adv.*, 2014, **4**, 1266–1269.

31 R. Yang, Y. Ji, Q. Li, Z. Zhao, R. Zhang, L. Liang, F. Liu, Y. Chen, S. Han and X. Yu, Ultrafine Si nanowires/Sn_3O_4 nanosheets 3D hierarchical heterostructured array as a photoanode with high-efficient photoelectrocatalytic performance, *Appl. Catal., B*, 2019, 117798.

32 S. Kulkarni, P. Patil, A. Mujumdar and J. Naik, Synthesis and evaluation of gas sensing properties of PANI, PANI/SnO_2 and PANI/SnO_2/rGO nanocomposites at room temperature, *Inorg. Chem. Commun.*, 2018, **96**, 90–96.

33 G. Gaikwad, P. Patil, D. Patil and J. Naik, Synthesis and evaluation of gas sensing properties of PANI based graphene oxide nanocomposites, *Mater. Sci. Eng., B*, 2017, **218**, 14–22.

34 D. Bandgar, G. Khuspe, R. Pawar, C. Lee and V. Patil, Facile and novel route for preparation of nanostructured polyaniline (PANI) thin films, *Appl. Nanosci.*, 2014, **4**, 27–36.

35 W. Jiang, Y. Liu, J. Wang, M. Zhang, W. Luo and Y. Zhu, Separation-free Polyaniline/TiO_2 3D hydrogel with high photocatalytic activity, *Adv. Mater. Interfaces*, 2016, **3**, 1500502.

36 M. Xu, J. Zhang, S. Wang, X. Guo, H. Xia, Y. Wang, S. Zhang, W. Huang and S. Wu, Gas sensing properties of SnO_2 hollow spheres/polythiophene inorganic–organic hybrids, *Sens. Actuators, B*, 2010, **146**, 8–13.

37 P. Manivel, S. Ramakrishnan, N. K. Kothurkar, A. Balamurugan, N. Ponpandian, D. Mangalaraj and C. Viswanathan, Optical and electrochemical studies of polyaniline/SnO_2 fibrous nanocomposites, *Mater. Res. Bull.*, 2013, **48**, 640–645.

38 W. Shao, F. Gu, L. Gai and C. Li, Planar scattering from hierarchical anatase TiO_2 nanoplates with variable shells to improve light harvesting in dye-sensitized solar cell, *Chem. Commun.*, 2011, **47**, 5046–5048.

39 Y. Lin, X. Wu, Y. Han, C. Yang, Y. Ma, C. Du, Q. Teng, H. Liu and Y. Zhong, Spatial separation of photogenerated carriers and enhanced photocatalytic performance on Ag_3PO_4 catalysts *via* coupling with PPy and MWCNTs, *Appl. Catal., B*, 2019, **258**, 117969.

40 F. Dong, W. K. Ho, S. Lee, Z. Wu, M. Fu, S. Zou and Y. Huang, Template-free fabrication and growth mechanism of uniform $(BiO)_2CO_3$ hierarchical hollow microspheres with outstanding photocatalytic activities under both UV and

visible light irradiation, *J. Mater. Chem.*, 2011, **21**, 12428–12436.

41 M. Mitra, A. Ghosh, A. Mondal, K. Kargupta, S. Ganguly and D. Banerjee, Facile synthesis of aluminium doped zinc oxide-polyaniline hybrids for photoluminescence and enhanced visible-light assisted photo-degradation of organic contaminants, *Appl. Surf. Sci.*, 2017, **402**, 418–428.

42 J. Liu, C. Wang and Q. Yang, Hydrothermal synthesis and gas-sensing properties of flower-like Sn_3O_4, *Sens. Actuators, B*, 2016, **224**, 128–133.

43 Y. Yang, Y. Wang and S. Yin, Oxygen vacancies confined in SnO_2 nanoparticles for desirable electronic structure and enhanced visible light photocatalytic activity, *Appl. Surf. Sci.*, 2017, **420**, 399–406.

44 M. Mitra, S. T. Ahamed, A. Ghosh, A. Mondal, K. Kargupta, S. Ganguly and D. Banerjee, Polyaniline/Reduced Graphene Oxide Composite-Enhanced Visible-Light-Driven Photocatalytic Activity for the Degradation of Organic Dyes, *ACS Omega*, 2019, **4**, 1623–1635.

45 S. Golczak, A. Kanciurzewska, M. Fahlman, K. Langer and J. Langer, Comparative XPS surface study of polyaniline thin films, *Solid State Ionics*, 2008, **179**, 2234–2239.

46 D. Wang, L. Yue, L. Guo, F. Fu, X. He and H. Shen, AgBr nanoparticles decorated $BiPO_4$ microrod: a novel p–n heterojunction with enhanced photocatalytic activities, *RSC Adv.*, 2015, **5**, 72830–72840.

47 X. Xu, R. Liu, Y. Cui, X. Liang, C. Lei, S. Meng, Y. Ma, Z. Lei and Z. Yang, PANI/FeUiO-66 nanohybrids with enhanced visible-light promoted photocatalytic activity for the selectively aerobic oxidation of aromatic alcohols, *Appl. Catal., B*, 2017, **210**, 484–494.

48 J. Li, T. Peng, Y. Zhang, C. Zhou and A. Zhu, Polyaniline modified SnO_2 nanoparticles for efficient photocatalytic reduction of aqueous Cr(VI) under visible light, *Sep. Purif. Technol.*, 2018, **201**, 120–129.

49 Y. Sheng, Z. Wei, H. Miao, W. Yao, H. Li and Y. Zhu, Enhanced organic pollutant photodegradation *via* adsorption/photocatalysis synergy using a 3D g-C_3N_4/TiO_2 free-separation photocatalyst, *Chem. Eng. J.*, 2019, **370**, 287–294.

50 K. S. W. Sing, J. Rouqerol and T. Siemieniewska, *Pure Appl. Chem.*, 1985, **57**, 603.

51 M. Karpuraranjith and S. Thambidurai, Biotemplate-SnO_2 particles intercalated PANI matrix: enhanced photo catalytic activity for degradation of MB and RY-15 dye, *Polym. Degrad. Stab.*, 2016, **133**, 108–118.

52 D. Geethalakshmi, N. Muthukumarasamy and R. Balasundaraprabhu, Effect of dopant concentration on the properties of HCl-doped PANI thin films prepared at different temperatures, *Optik*, 2014, **125**, 1307–1310.

53 Y. Wang, Q. Wang, X. Zhan, F. Wang, M. Safdar and J. He, Visible light driven type II heterostructures and their enhanced photocatalysis properties: a review, *Nanoscale*, 2013, **5**, 8326–8339.

54 X. Ma, J. Shen, D. Hu, L. Sun, Y. Chen, M. Liu, C. Li and S. Ruan, Preparation of three-dimensional Ce-doped Sn_3O_4 hierarchical microsphere and its application on formaldehyde gas sensor, *J. Alloys Compd.*, 2017, **726**, 1092–1100.

55 J. Wang, N. Umezawa and H. Hosono, Mixed valence tin oxides as novel van der Waals materials: theoretical predictions and potential applications, *Adv. Energy Mater.*, 2016, **6**, 1501190.

56 T. Q. Nguyen, A. K. Thapa, V. K. Vendra, J. B. Jasinski, G. U. Sumanasekera and M. K. Sunkara, High rate capacity retention of binder-free, tin oxide nanowire arrays using thin titania and alumina coatings, *RSC Adv.*, 2014, **4**, 3312–3317.

57 Q. Wang, J. Hui, J. Li, Y. Cai, S. Yin, F. Wang and B. Su, Photodegradation of methyl orange with PANI-modified BiOCl photocatalyst under visible light irradiation, *Appl. Surf. Sci.*, 2013, **283**, 577–583.

58 H. Zhang and Y. Zhu, Significant Visible Photoactivity and Antiphotocorrosion Performance of CdS Photocatalysts after Monolayer Polyaniline Hybridization, *J. Phys. Chem. C*, 2010, **114**, 5822–5826.

59 W. Yuan, C. Zhang, W. Hong, Q. Wang and K. Li, In situ synthesis and immobilization of a Cu(II)–pyridyl complex on silica microspheres as a novel Fenton-like catalyst for RhB degradation at near-neutral pH, *RSC Adv.*, 2017, **7**, 22825–22835.

60 S. C. Yan, Z. S. Li and Z. G. Zou, Photodegradation of rhodamine B and methyl orange over boron-doped g-C_3N_4 under visible light irradiation, *Langmuir*, 2010, **26**, 3894–3901.

61 H. Tang, D. Zhang, G. Tang, X. Ji, C. Li, X. Yan and Q. Wu, Low temperature synthesis and photocatalytic properties of mesoporous TiO_2 nanospheres, *J. Alloys Compd.*, 2014, **591**, 52–57.

62 F. Gao, Y. Cheng, L. An, R. Tan, X. Li and G. Wang, Polyaniline nanotube-ZnO composite materials: facile synthesis and application, *J. Wuhan Univ. Technol.*, 2015, **30**, 1147–1151.

63 M. Zhang, W. Jiang, D. Liu, J. Wang, Y. Liu and Y. Zhu, Photodegradation of phenol *via* C_3N_4-agar hybrid hydrogel 3D photocatalysts with free separation, *Appl. Catal., B*, 2016, **183**, 263–268.

64 H. Zhang, R. Zong and Y. Zhu, Photocorrosion Inhibition and Photoactivity Enhancement for Zinc Oxide *via* Hybridization with Monolayer Polyaniline, *J. Phys. Chem. C*, 2009, **113**, 4605–4611.

65 W. Jiang, W. Luo, R. Zong, W. Yao, Z. Li and Y. Zhu, Polyaniline/Carbon Nitride Nanosheets Composite Hydrogel: A Separation-Free and High-Efficient Photocatalyst with 3D Hierarchical Structure, *Small*, 2016, **12**, 4370–4378.

66 Y. Lv, W. Yao, X. Ma, C. Pan, R. Zong and Y. Zhu, The surface oxygen vacancy induced visible activity and enhanced UV activity of a ZnO_{1-x} photocatalyst, *Catal. Sci. Technol.*, 2013, **3**, 3136–3146.

67 W. Jiang, W. Luo, R. Zong, W. Yao, Z. Li and Y. Zhu, Polyaniline/Carbon Nitride Nanosheets Composite Hydrogel: A Separation-Free and High-Efficient

Photocatalyst with 3D Hierarchical Structure, *Small*, 2016, **12**, 4370–4378.

68 M. Mitra, A. Ghosh, A. Mondal, K. Kargupta and D. Banerjee, Facile synthesis of aluminium doped zinc oxide-polyaniline hybrids for photoluminescence and enhanced visible-light assisted photo-degradation of organic contaminants, *Appl. Surf. Sci.*, 2017, **402**, 418–428.

69 Y. Yao, J. Qin, H. Chen, F. Wei and X. Liu, One-pot approach for synthesis of N-doped $TiO_2/ZnFe_2O_4$ hybrid as an efficient photocatalyst for degradation of aqueous organic pollutants, *J. Hazard. Mater.*, 2015, **291**, 28–37.

70 D. Liu, J. Wang, Y. Wang and Y. Zhu, An anion exchange strategy for construction of a novel Bi_2SiO_5/Bi_2MoO_6 heterostructure with enhanced photocatalytic performance, *Catal. Sci. Technol.*, 2018, **8**, 3278–3285.

71 D. Wang, L. Yue, L. Guo, F. Fu, X. He and H. Shen, AgBr nanoparticles decorated $BiPO_4$ microrod: a novel p–n heterojunction with enhanced photocatalytic activities, *RSC Adv.*, 2015, **5**, 72830–72840.

72 C. B. Hiragond, P. K. Khanna and P. V. More, Probing the real-time photocatalytic activity of CdS QDs sensitized conducting polymers: featured PTh, PPy and PANI, *Vacuum*, 2018, **155**, 159–168.

73 J. Ren, S. Ouyang, H. Chen, N. Umezawa, D. Lu, D. Wang, H. Xu and J. Ye, Effective mineralization of organic dye under visible-light irradiation over electronic-structure-modulated $Sn(Nb_{1-x}Ta_x)_2O_6$ solid solutions, *Appl. Catal., B*, 2015, **168**, 243–249.

74 S. Steplin Paul Selvin, A. Ganesh Kumar, L. Sarala, R. Rajaram, A. Sathiyan, J. Princy Merlin and I. Sharmila Lydia, Photocatalytic degradation of rhodamine B using zinc oxide activated charcoal polyaniline nanocomposite and its survival assessment using aquatic animal model, *ACS Sustainable Chem. Eng.*, 2017, **6**, 258–267.

75 S. Sharma, S. Singh and N. Khare, Synthesis of polyaniline/CdS (nanoflowers and nanorods) nanocomposites: a comparative study towards enhanced photocatalytic activity for degradation of organic dye, *Colloid Polym. Sci.*, 2016, **294**, 917–926.

76 E. R. Carraway, A. J. Hoffman and M. R. Hoffmann, Photocatalytic oxidation of organic acids on quantum-sized semiconductor colloids, *Environ. Sci. Technol.*, 1994, **28**, 786–793.

77 Z. Xiong, L. Ji, S. Zhang and W. Yang, Synthesis of a novel polyaniline-intercalated layered manganese oxide nanocomposite as electrode material for electrochemical capacitor, *J. Power Sources*, 2007, **173**, 1017–1023.

78 M. J. Chatterjee, A. Ghosh, A. Mondal and D. Banerjee, Polyaniline–single walled carbon nanotube composite – a photocatalyst to degrade rose bengal and methyl orange dyes under visible-light illumination, *RSC Adv.*, 2017, **7**, 36403–36415.

79 L. Dong, W. Xue, J. Deng, C. Zhou, J. Guo and L. Peng, Crosslinked Carbon Nanotubes/Polyaniline Composites as a Pseudocapacitive Material with High Cycling Stability, *Nanomaterials*, 2015, **5**, 1034–1047.